POLITECNICO
MILANO 1863

Modeling of a blow-down propulsion system

Course of Space Propulsion
Academic Year 2023-2024

Lockheed Martini Group

Alessandro Pallotta	alessandro1.pallotta@mail.polimi.it	10712370
Alex Cristian Turcu	alexcristian.turcu@mail.polimi.it	10711624
Chiara Poli	chiara3.poli@mail.polimi.it	10731504
Daniele Paternoster	daniele.paternoster@mail.polimi.it	10836125
Paolo Vanelli	paolo.vanelli@mail.polimi.it	10730510
Riccardo Vidari	riccardo.vidari@mail.polimi.it	10711828

Contents

Nomenclature

Acronyms

AM	Additive Manufacturing	**LRE**	Liquid Rocket Engine
BJ	Binder Jetting	**RP-1**	RP-1 fuel
LOX	Liquid Oxygen	**TBC**	Thermal Barrier Coating
LPBF	Laser Powder Bed Fusion		

Symbols

a	[m/s]	Speed of sound
A	[m^2]	Area
B	[-]	Blow-down ratio
c	[J/kg K]	Specific heat
c_P	[J/kg K]	Specific heat at constant pressure
c_T	[-]	Thrust coefficient
c^*	[m/s]	Characteristic velocity
C_d	[-]	Discharge coefficient
D	[m]	Diameter
E	[m/s]	Erosion rate
f	[-]	Darcy friction factor
h_g	[W/m^2 K]	Gas-side convective heat transfer coefficient
H	[m]	Height
i	[-]	First iteration index
I_{sp}	[s]	Specific impulse
I_{tot}	[N s]	Total impulse
j	[-]	Second iteration index
k	[m]	Radius of curvature
K	[-]	Pressure loss coefficient
L	[m]	Length
L^*	[m]	Characteristic length
m	[kg]	Mass
$\dot{m}$	[m/s]	Mass flow rate
M	[-]	Mach number
$\mathbb{M}$	[kg/mol]	Molar mass
N	[-]	Number of
O/F	[-]	Oxidizer to fuel ratio
$\overline{O/F}$	[-]	Mean O/F ratio
p	[Pa]	Pressure
Δp	[Pa]	Pressure loss / difference
Pr	[-]	Prandtl number
$\dot{q}$	[W/m^2]	Heat flux
$\dot{Q}$	[W]	Heat transfer rate
r	[-]	Recovery factor
R	[J/kg K]	Specific gas constant
$\mathcal{R}$	[J/mol K]	Universal gas constant
Re	[-]	Reynolds number
Re'	[-]	Modified Reynolds number
t	[s]	Time
Δt	[s]	Time step
T	[K]	Temperature
ΔT	[K]	Variation of temperature
$\mathbb{T}$	[N]	Thrust
u	[m/s]	Velocity
V	[m^3]	Volume
ΔV	[m^3]	Volume change
α_{AM}	[deg]	Deposition angle of AM
α_{con}	[deg]	Convergent semi-aperture angle
β	[%]	Injector pressure drop as percentage of initial combustion chamber pressure
γ	[-]	Heat capacity ratio
δ	[deg]	Cone angle of fictitious conical divergent
ε	[-]	Area ratio
θ	[deg]	Angle of Rao parabolic divergent
λ	[-]	Nozzle losses coefficient
μ	[Pa s]	Dynamic viscosity
ρ	[kg/m^3]	Density
σ	[-]	Correction factor across boundary layer

Subscripts

aw	Adiabatic wall	**id**	Ideal
b	Burn	**inj**	Injector
c	Combustion chamber	**max**	Maximum
cea	From CEAM software	**min**	Minimum
co	Coolant	**ox**	Oxidizer
con	Convergent	**p**	Propellants
div	Divergent	**pr**	Pressurizer gas
e	Nozzle exit	**r**	Real
eff	Effective	**t**	Nozzle throat
f	Final	**tc**	Thrust chamber
fd	Feeding lines	**tk**	Tank
fu	Fuel	**tot**	Total
i	Initial	**wg**	Gas side wall

1 Introduction and literature overview

In this work a preliminary design of a 1 kN semi-cryogenic LRE (LOX/RP-1) equipped with a blow-down feeding system is discussed. In particular, a first literature analysis was done in order to review previous studies regarding this particular architecture. Recent developments in additive manufacture (AM) techniques were analyzed to obtain some knowledge regarding processes and precision of this new frontier. Moreover, due the reduced size of this system, some criticalities regarding boundary layer and erosion losses were researched. The second part of the paper aim at designing the engine with some imposed initial conditions and some assumptions. The whole dimensioning of the system, including the tanks and feeding lines, is carried on including the dynamics of the system. The final sizing will accomplish the maximization of the total impulse, with the initial and final constraints. An off-design analysis is then performed to quantify the performances with nozzle losses and AM uncertainties. Finally, a feasibility analysis of nozzle fuel cooling is discussed.

1.1 Blow-down heritage

The blow-down architecture is the simplest feeding technique for LRE since it does not require additional pressurizing gas tanks with failure-prone pressure regulator valves nor complex turbomachinery. The scheme includes only two liquid propellant tanks filled with helium or nitrogen, eventually separated by a membrane. The major downsides of this simplicity is relative to the non-stationarity of the tank pressures that induce chamber pressure drop, decrease of propellant mass flow rate and as a consequence O/F ratio variation. This chain of events degrades performances overtime and must be carefully evaluated since combustion efficiency relies upon viable domains of injection pressure and correct mass flow ratio. The interest on blow-down is although justified with respect to well-known pressure regulated feed system since this last can also manifest some criticalities in terms of long-term reliability. In particular, propulsion systems play crucial roles for mission success, such as long interplanetary trips, and they must ensure failure-free lifetime. This is a major concern when focusing on pressure regulated feeding lines in which a pressure regulator valve is present. This kind of elements can be quite complex and hence add a weakness for the whole system[1]. Considering these facts, a blow-down type architecture could be of interest since it decrease system complexity. Moreover, different feasibility analysis for blow-down units are present in the literature in which also an external re-pressurization tank is considered[2]. This is an upgrade that allows to recover performance of the feeding pressure and hence combustion properties. Although the valve complexity is removed since a pyro valve can be used to discharge the gas with a single shot application, the eventual re-pressurization can be a crucial point as the sudden change in pressure could induce unwanted instabilities. Other configurations could foresee the use of a Venturi valve to maintain constant mass flow rate by cavitating the liquid and choking the flow on the feeding line. However, neither extra tank nor Venturi valves will be considered in this work in order to meet the requirements presented in subsection 2.1.

The whole evaluation of the dynamics of the examined propulsion system was not based upon previous works, instead a self-made model was developed.

1.2 Additive manufacturing state of art

Additive manufacturing technologies in aerospace industry is rapidly spreading thanks to the offered advantages with respect to traditional production techniques. Among the benefits provided by AM there are weight and time savings, cost reductions and the possibility to optimize components creating more complex geometries[3]. Various technologies for AM have been developed for different fields, in particular, the most used in this sector is Laser Powder Bed Fusion (LPBF), which utilizes a laser beam to melt successive layers of metal powder. Binder Jetting (BJ) is also a feasible technology although still under development, as it requires post-processing procedures to obtain better finished components than LPBF, making it less attractive for the general industry. A focus on this technology will be carried on in the following pages. Different types of alloys can be processed through both technologies, among which there are nickel-based superalloys, such as Inconel-718. This materials offers excellent mechanical properties under extreme temperature conditions and, for this precise reason, suits perfectly the role of injectors, manifolds and turbomachinery elements in general. Inconel-718 is also characterized by a considerable corrosion resistance, that allows it to be used in concomitance with an oxidizer such as liquid oxygen[4].

The finishing of a component created with AM depends on several parameters:

- **Temperature**: the laser's power and thus the powder's melting temperature selection is crucial in order

to avoid performance losses due to stress induced by heating and cooling cycles. The calculation of this parameter is important to prevent overflowing from the meltpool, convective transport of the liquid and nonmetal particles to be blown away from vapors. Cracks and curling, caused by uneven shrinkage during production can also damage surface quality[5].

- **Powder dimension and morphology**: the mechanical properties of the component are significantly influenced by the dimensions and shape of the powder. Coarse and irregular particles result in inefficient packing and higher porosity of the powder bed. This, in turn, makes it challenging for the molten material to fill all the interstices, especially due to the rapid solidification in the LPBF process. The mechanical properties of the component decrease due to its porosity[6].

- **Deposition method**: powder deposition direction directly affects the superficial finishing of the material as dross or deposits from the process can be present: the angle of deposition directly influences the roughness and the accuracy of the produced parts. Staircase effects is related to the discretization of the different layers: the bigger the layers the less smooth the surface will be. In general, it can be observed that the more the build direction α of a generic piece shifts from perpendicular ($\alpha = 0°$), to parallel, ($\alpha = 90°$), the roughness increases and accuracy lowers[7].

BJ is a technology firstly developed during the nineties and consists in a deposition of a polymeric liquid binder onto successive layers of powder. The whole process takes place at ambient temperature and pressure. No controlled atmosphere is required as phase changes are not involved in this process. The binder bonds the different layers together without needing of supports, resulting in a box of powder with a 3D component built inside. Post processing treatments, such as sintering and infiltration, are performed to improve its properties[8]. On the contrary, LPBF technology uses an high power laser beam to melt the different layers of powder together. A more controlled ambient and atmosphere are required as thermal stresses play a major role during the production of different items[3].

BJ technology technology brings advantages and disadvantages with respect to LPBF:

- **Material compatibility**: BJ is potentially compatible with any material, metallic and non metallic, allowing to build complex components, unfeasible with LPBF process capabilities.

- **Roughness**: BJ technologies require a significant amount of post processing treatments to improve both superficial finishing and mechanical properties, reaching lower values of roughness with respect to LPBF. In general, fewer superficial treatments are required by LPBF as the layer stratification could lead to more accurate roughness. Refinement is instead necessary with BJ-made components to obtain lowest possible values of roughness, even better than the ones LPBF could reach. BJ components show average roughness of $\approx 6\,\mu m$, lower than the one obtained with LPBF printing, spacing between 70 and 10 μm[7]. It's important to note that the roughness of BJ-made components is less dependant on the build direction α.

- **Density drawback**: BJ-made component show lower relative densities leading to possible distortions of the printed elements. Again, post-processing is required with sintering at temperatures of $\approx 1300°$.

- **Mass production**: Production of components via BJ is more cost and time effective in case of batches of multiple parts.

- **Shrinkage**: metal parts produced with BJ can shrink by up to 2 % for smaller items and by more than 3% for larger items as a result of infiltration. Sintering can cause average shrinkage of 20% and also lead to warping caused by friction between the furnace plate and the bottom surface of the part. The heat used in sintering can also soften the part and cause unsupported areas to deform under their own weight. While these problems can be compensated for in the build, non-uniform shrinkage can be more difficult to account for[9].

Even if BJ is a promising technology, more sustainable as it produces less wastes and requires less energy in the production of different pieces, it lacks a solid mathematical modelling[8] as the research dedicated to this technology is still in its infancy. LPBF is thus the technology of choice to build the systems of DRY-1.

1.3 Analysis of losses

The model of the system was based on some ideal assumption of the propulsion process, but in the nozzle some irreversible processes and losses are present. Therefore some of them were analyzed and compared with the ideal case to achieve a better understanding of what really happens in the nozzle. The losses considered are

specifically the ones caused by 2D flow, throat erosion and boundary layer. Considering 2D flow means that the propellants exit velocity is slightly misaligned from the nozzle axis, especially near its edges. Therefore only part of the flow will contribute to the thrust of the engine. The throat erosion is mostly caused by the exhaust gasses passing through it with high velocity and temperature, thus causing the material of the nozzle to erode and fail more easily. This effect causes an unwanted expansion of the throat area during the mission consequently increasing the rate at which the combustion chamber pressure decreases over time. The boundary layer loss is caused by the presence of a boundary layer between the nozzle wall and the flowing gasses. It is present along the whole nozzle but its effects are particularly evident in the throat, as it is the smallest part of the nozzle. This effect is accentuated even more by general dimensions of the considered system.

2 Modelling of propulsion system: DRY-1

The workflow for the sizing of DRY-1 is introduced by Figure 1 and it is divided into three stages:

- **Input data**: the problem is set up.
- **Nominal sizing**: the system is sized according to initial conditions and general assumptions.
- **System dynamics**: an iterative process is set up to model the blow-down dynamics and finalize the sizing.
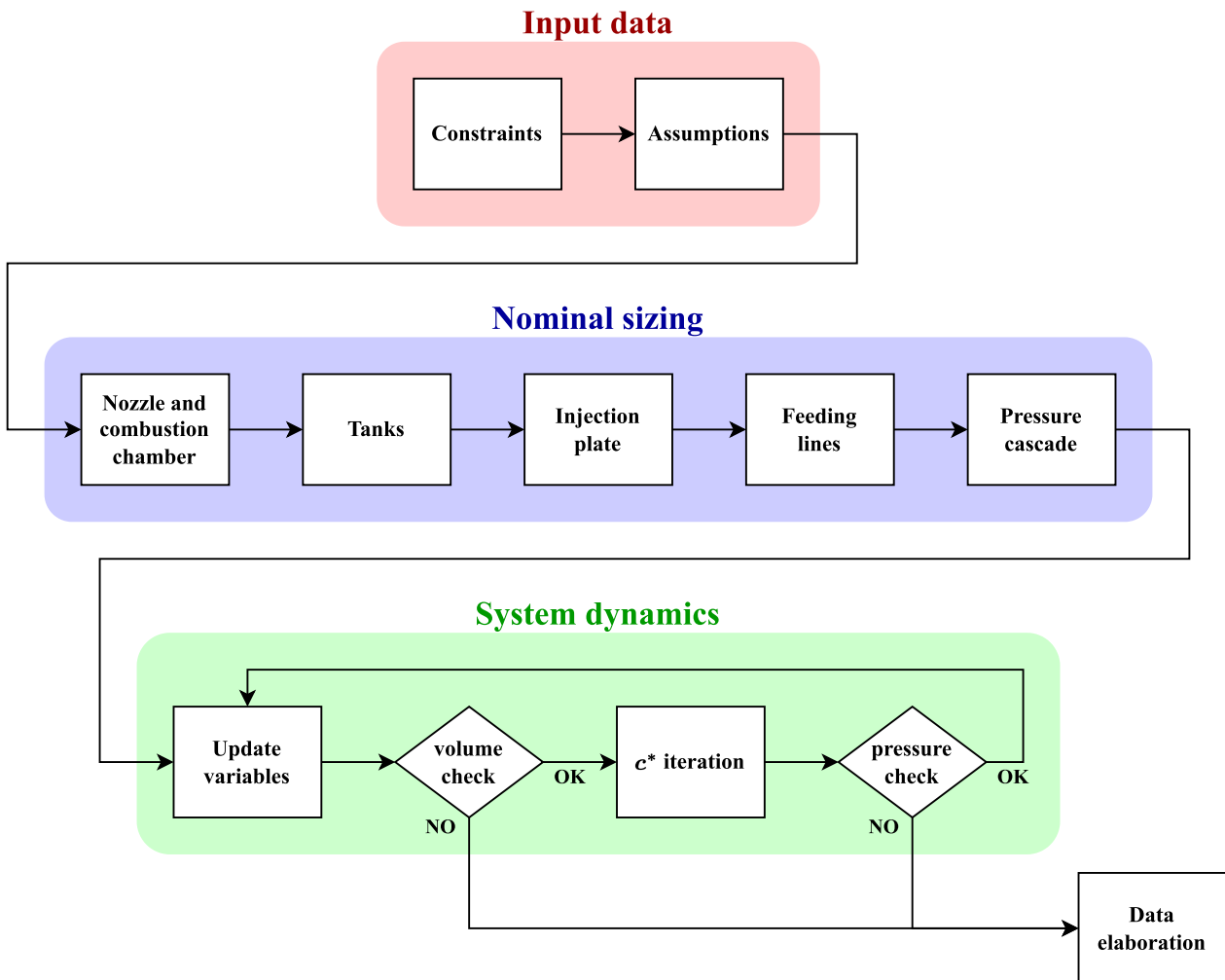

Figure 1: Flowchart of the simulation model

2.1 Input data

The input data defined different kind of requirements, related to operability environment, engine performance, size constraints, chemistry, architecture and manufacturing techniques. Regardless of the development of the engine design, the system shall respect the following pinpoints:

- **Environment**: vacuum for the whole operation.

- **Thrust** $\mathbb{T}$: initial magnitude of 1 kN, no lower boundary.
- **Chamber pressure** p_c: initial value of 50 bar, always above 20 bar throughout the whole mission.
- **Allocated space**: tanks, combustion chamber and convergent nozzle occupancy is exactly 80% of the volume occupied by a cylinder of 1 meter diameter and 2 meter length. No bounds on the extension of the divergent.
- **Propellants**: semi-cryogenic couple of LOX and RP-1.
- **Architecture**: blow-down type.
- **Manufacturing**: all the system is produced in AM, no restriction on material nor techniques.

The nominal sizing refers to the design of the overall system considering the imposed initial constraints as static conditions. This design choice was dictated by the dynamics of the blow-down system, which imposes the maximum flow rate at the beginning of the mission, leading to the oversizing of the engine throughout the rest of the mission.

Various hypothesis were necessary to develop the system, this values are reported in Table 1.

O/F [-]	ε [-]	ε_{con} [-]	L^* [m]	D_{inj}^{fu} [mm]
2.42	300	10	1.143	1

Table 1: Hypothesis from literature and previous design

The choices of L^* and O/F were only dictated by the propellant couple[10], while ε was chosen as the characteristic of the engine refers to an in-space application[11]. Regarding the value of ε_{con} a mean value between 5 and 15 was taken. Smaller values entails longer combustion chamber and small cross sectional area, with large pressure drops. Larger values refers to bigger chamber cross sectional area, with limited length for the combustion. From the literature the suggestion for the choice of this value is to refer to previous successful engines design, considering the same application[12]. Therefore, a 400 N bi-propellant apogee motor was taken as reference and revealed a value of $\varepsilon_{con} \approx 10$[11].

2.2 Nominal sizing

After defining the main input data, the workflow is carried out as shown in Figure 1. All the combustion simulations were performed with Nasa-CEA software, implemented in Matlab (CEAM). In particular the "rocket problem" was considered, Bray model was applied for the expansion (frozen point at the throat), infinite combustion chamber ($M_c = 0$), initial injecting temperatures of the propellant equal to the storage temperatures. The chamber pressure was set as $p_c = 50$ bar and the mixture ratio as $O/F = 2.42$. Latter refinement of this last value will be performed. The output values used from the simulation are represented in table Table 2 (vacuum value is considered for the c_T):

c^* [m/s]	c_T [-]	T_c [K]	γ_c [-]	I_{sp} [s]
1851.0	1.935	3709	1.1405	365.22

Table 2: First run on CEAM

From this results, the propellant mass flow rate and the throat area can be calculated:

$$\dot{m}_p = \frac{\mathbb{T}}{c_T c^*} \qquad A_t = \frac{\dot{m}_p c^*}{P_c} \tag{1}$$

From the geometry assumption of Table 1, the nozzle exit area and the combustion chamber geometry can be retrieved:

$$A_e = \varepsilon A_t \tag{2}$$

$$A_c = \varepsilon_{con} A_t \qquad L_c = \frac{L^*}{\varepsilon_{con}} \tag{3}$$

$\dot{m}_p$ [kg/s]	D_t [cm]	D_e [cm]	D_c [cm]	L_c [cm]
0.279	1.15	19.86	3.63	11.43

Table 3: Preliminary DRY-1 geometry

The nozzle geometry was modelled with a conical convergent and a Rao parabolic divergent[13]. For the convergent a realistic cone angle of $\alpha_{con} = 30°$ was chosen from which its length can be computed.

$$L_{con} = \frac{D_c - D_t}{2\tan(\alpha_{con})} \tag{4}$$

Since no constraint was imposed on the divergent length a 100% bell percentage was selected in order to minimize 2D losses as described in section 4. From it, together with the area ratio, the parabolic nozzle can be defined. The nozzle's main characteristics are reported in Table 4

L_{con} [cm]	L_{div} [cm]	θ_e [deg]
2.15	34.91	4.329

Table 4: Nozzle main characteristics

A simplified geometrical model of the whole system is shown in Figure 2:
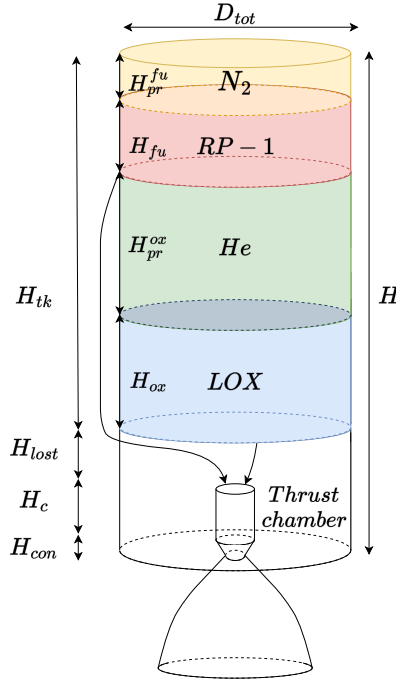
Figure 2: System configuration

A check on the compliance of the chamber Mach number is done ($M_c < 0.3$):

$$\frac{1}{\varepsilon_{con}} = M_c \left[\frac{1 + \frac{\gamma_c - 1}{2}}{1 + \frac{\gamma_c - 1}{2} M_c^2} \right]^{\frac{\gamma_c + 1}{2(\gamma_c - 1)}} \qquad \xrightarrow{fsolve} \qquad M_c = 0.059 \tag{5}$$

From the geometry of the motor and the allocated space constraints, the total height of the tanks can be calculated. The volume around the thrust chamber (combustion chamber + convergent) can be assessed:

$$V_{tc} = \frac{\pi}{4} \left[L_c D_c^2 + \frac{L_{con}}{3} \left(D_c^2 + D_t^2 + D_c D_t \right) \right] \tag{6}$$

Also, the volume of the cylinder that covers the length of the thrust chamber and with the total diameter of 1 meter (D_{tot}) can be computed. From there, the empty volume around the thrust chamber can be computed as a difference:

$$V_{lost} = V_{tc} - \frac{\pi}{4}(L_c + L_{con})D_{tot} \tag{7}$$

This value must be 20% of the total cylinder volume, as cited in subsection 2.1. As the computed value was lower, additional volume had to be removed from the tanks in order to meet the requirement. The height dedicated to the tanks is calculated as follow:

$$H_{tk} = H - \left[L_c + L_{con} + \frac{4}{\pi D_{tot}^2}(0.2V_{tot} - V_{lost}) \right] \tag{8}$$

The total volume allocated to the tanks is hence fully defined. In order to calculate the masses of pressurizer and propellants, some assumption have to be made:

- adiabatic expansion of the pressurizing gas;
- blow-down ratios can be tuned;
- mean value of the oxidizer to fuel ratio.

A system of equations can be set up:

$$\begin{cases} \dfrac{m_{ox}}{m_{fu}} = \overline{O/F} \\ m_{ox} = \rho_{ox}V_{ox} \\ m_{fu} = \rho_{fu}V_{fu} \\ V_{ox} = V_{pr,f}^{ox} - V_{pr,i}^{ox} \\ V_{fu} = V_{pr,f}^{fu} - V_{pr,i}^{fu} \\ V_{pr,f}^{ox} = B_{ox}^{\frac{1}{\gamma_{pr,ox}}} V_{pr,i}^{ox} \\ V_{pr,f}^{fu} = B_{fu}^{\frac{1}{\gamma_{pr,fu}}} V_{pr,i}^{fu} \end{cases} \tag{9}$$

In order to solve System 9, the pressurizer and the initial temperature of the propellants have to be set. Different pressurizing gas are available, mainly nitrogen or helium are the most common choices. The main differences for the two are the storage temperature, the molar mass and the specific heat ratio. The latter parameter influences the adiabatic discharge, higher values implies faster pressure discharge. The molar mass affects the amount of gas to be embarked at a given pressure. The storage temperature is a matter of compatibility with the propellant. Nitrogen gas was chosen to pressurize RP-1 since no cryogenic conditions were present also it guarantees lower discharge, with the downside of increasing the mass of the system. On the other side, LOX required a cryogenic compatibility that can be ensured by helium. Even though an efficient insulating bladder is employed, the design choice was dictated by a more conservative approach. The employment of nitrogen also with LOX was discarded since storage temperature and pressure are not compatible with its properties[14].

T_{pr}^{fu} [K]	T_{pr}^{ox} [K]	γ_{N_2} [-]	γ_{He} [-]
300	90	1.40	1.67

Table 5: Initial values for pressurizer gases and specific heat ratio values

$\overline{O/F}$ [-]	$B_{pr,ox}$ [-]	$B_{pr,fu}$ [-]	V_{tot} [m^3]
2.42	2.5	2.5	1.27

Table 6: Assumed or calculated values as first iteration

The blow-down ratios B_{pr} are initially chosen assuming negligible losses and according to the boundaries imposed by the combustion chamber, as stated in subsection 2.1. This particular element deeply influences the whole dynamics and there were no reasons to set two different B_{pr}. The masses and volumes of oxidizer, fuel and pressurizing gases are then computed.

m_{fu} [kg]	m_{ox} [kg]	$V_{pr,i}^{fu}$ [m³]	$V_{pr,i}^{ox}$ [m³]	$V_{fu,i}$ [m³]	$V_{ox,i}$ [m³]
165.34	400.13	0.2217	0.4789	0.2049	0.3510

Table 7: Propellant and pressurizer quantities as first iteration

Finally, the feeding lines and the injectors plate of DRY-1 can be modelled. Considering Figure 2, the length of the pipes can be retrieved as a difference:

$$L_{fd}^{fu} = H - L_c - H_{tk,fu} \tag{10}$$

$$L_{fd}^{ox} = H - L_c - H_{tk} \tag{11}$$

The initial pressure drop across the injector Δp_{inj} has to be assumed as a percentage of the initial chamber pressure. An acceptable range of this fraction goes from 5% to 30%. A value of 20% is chosen for both oxidizer and fuel lines. The fuel and oxidizer injectors' area can be computed assuming reasonable values for the discharge coefficient $C_{d,inj}$. A fair assumption has been made according to the superficial roughness quality of AM as explained in section 5.

$$\dot{m}_{fu} = \frac{1}{1 + O/F}\dot{m}_p \qquad \dot{m}_{ox} = \frac{O/F}{1 + O/F}\dot{m}_p \tag{12}$$

$$A_{inj}^p = \frac{\dot{m}_p}{C_{d,inj}\sqrt{2\Delta p_{inj}\rho_p}} \tag{13}$$

Note that A_{inj}^p is referred or to fuel's injectors area or to oxidizer's injectors area calculated by the imposed conditions.

By assuming a diameter for the fuel injector (Table 1), the number of injectors can be computed:

$$A_{inj,single}^{fu} = \frac{\pi D_{inj}^{fu\,2}}{4} \tag{14}$$

$$N_{inj}^{fu} = \left\lfloor \frac{A_{inj,fu}}{A_{inj,single\,fu}} \right\rfloor \tag{15}$$

For the injection plate, short tubes with conical entrance are assumed (see discussion in section 5) in a triplet configuration, matching as much as possible the predicted $\overline{O/F}$.

$$N_{inj}^{ox} = 2 \cdot N_{inj}^{fu} \tag{16}$$

The real A_{inj} will influence the diameters of the injectors, making them different from the supposed one. New values for the injectors diameters shall be calculated to respect the imposed A_{inj}. Final results are reported in Table 8.

N_{inj}^{fu} [−]	N_{inj}^{ox} [−]	D_{inj}^{fu} [mm]	D_{inj}^{fu} [mm]
3	6	1.12	1.13

Table 8: Propellant and pressurizer quantities as first iteration

Once the the geometry of the injection plate is established, feeding line losses were modelled. As shown in Equation 18, the dimension of the lines and the Darcy friction factor f are needed. This last coefficient depends on the Re and on the roughness and it is retrieved from Moody chart[15].

The speed of the fluid inside the lines is found from the mass flow rate and thus the losses along the whole system are computed via Equation 17, Equation 18, Equation 19. The diameter of the two feeding lines is assumed to be different to counter balance the effect of the different densities of the fluids.

D_{fd}^{fu} [mm]	D_{fd}^{ox} [mm]
5	7

Table 9: Diameter assumed for feeding lines

$$u_{p,fd} = \frac{\dot{m}_p}{A_{p,fd}\rho_p} \tag{17}$$

$$K_{p,tot} = 1 + f\frac{L_{p,fd}}{D_{p,fd}} + \left(\frac{A_{p,fd}}{A_{p,inj,tot}C_{d,inj}}\right)^2 \tag{18}$$

$$\Delta p_p = \frac{1}{2}\rho_p k_{p,tot}u_{p,fd}^2 \tag{19}$$

Finally, the pressure inside the tanks can be computed. This value will influence the whole dynamics of the system and will be refined to maximize the total impulse.

$p_{fu,i}$ [bar]	$p_{ox,i}$ [bar]
60.79	60.19

Table 10: Initial tank pressure

As can be seen, values are similar between the two tanks despite the difference in fluid density, pipe length and pipe diameter, as the pressure cascade in a such compact system is mainly driven by the imposed pressure drop across the injectors, imposed to be equal.
Results of the nominal design will be presented in section 3.

2.3 System dynamics

From the nominal sizing of the engine, it is necessary to simulate the real dynamics of the system in order to:

- retrieve the performance of the designed system in time;
- check the compliance of the system with the constraints;
- test other designs through iteration to select the best one based on the simulated data of interest.

For this reasons, a numerical method was implemented. An high level explanation for the functioning of the algorithm can be appreciated in Figure 3.
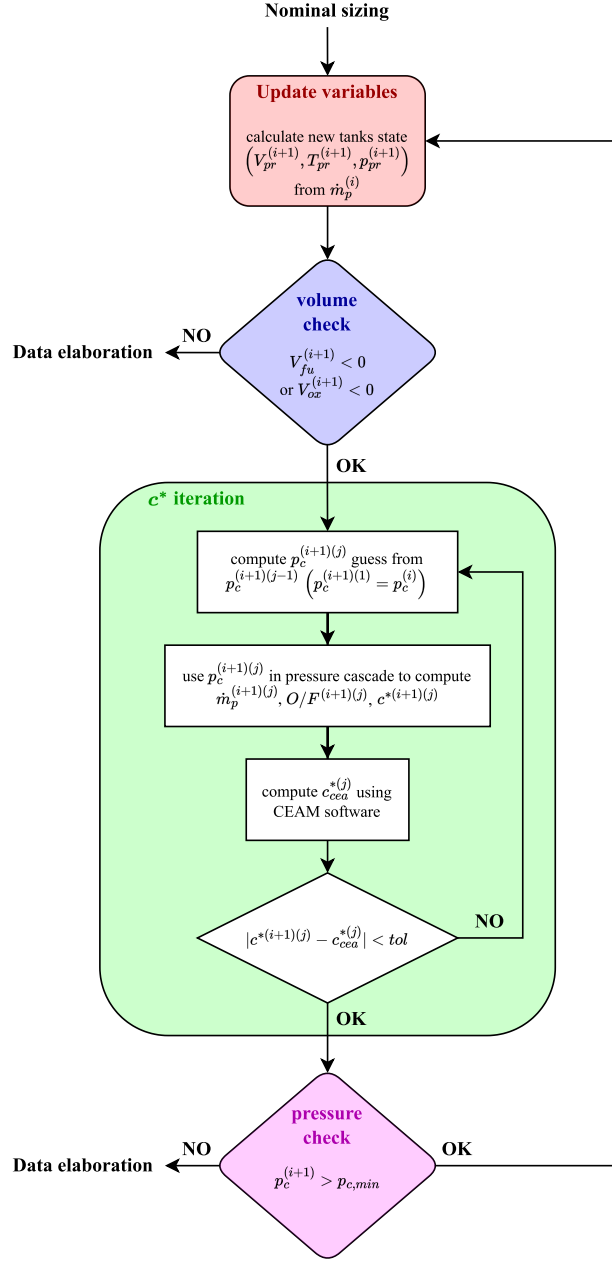
Figure 3: Flowchart of dynamics of the model

The first step of the time cycle is to update the state of the two tanks based on the previous iteration. Assuming a constant propellants flow rate during the time step Δt, the volume of the remaining liquid is decreased by a quantity $\Delta V^{(i+1)}$. Accordingly, the volume of the pressurizer will increase by the same amount.

$$\Delta V^{(i+1)} = \frac{\dot{m}_p^{(i)} \Delta t}{\rho_p} \tag{20}$$

$$V_p^{(i+1)} = V_p^{(i)} - \Delta V^{(i+1)} \tag{21}$$

$$V_{pr}^{(i+1)} = V_{pr}^{(i)} + \Delta V^{(i+1)} \tag{22}$$

From the change of volume, the new pressure and temperature of the pressurizer gas are computed assuming

an adiabatic expansion in the tank:

$$p_{pr}^{(i+1)} = p_{pr}^{(i)} \left(\frac{V_{pr}^{(i)}}{V_{pr}^{(i+1)}} \right)^{\gamma_{pr}} \tag{23}$$

$$T_{pr}^{(i+1)} = T_{pr}^{(i)} \left(\frac{V_{pr}^{(i)}}{V_{pr}^{(i+1)}} \right)^{\gamma_{pr}-1} \tag{24}$$

A check must be performed on the remaining volume of propellants in the tanks at current iteration: if the volume of fuel is negative it means that the combustion is over so the simulation stops (the same for oxidizer). If there is some more propellant to use, the iteration goes on with the calculation of the new chamber pressure. This step is complex because it introduces another cycle of iterations inside each time step. The mass flow rate of the propellants depends on the pressure cascade in the feeding lines, hence on the chamber pressure. These two variables are bounded and both unknown, but there's only one configuration that can match the boundary condition imposed by the critical condition in the throat, so the problem is well-posed.

From literature, the c^* of the chamber has the following expression:

$$c^* = \frac{p_c A_t}{\dot{m}_{fu} + \dot{m}_{ox}} \tag{25}$$

It correlates the chamber pressure with the propellants flow rate in the throat. Moreover, it only depends on the thermodynamics of the combustion process in the chamber, which changes over time due to the architecture of blow-down system. By imposing the critical conditions in the throat, it can be rewritten as:

$$c^* = \sqrt{\frac{\mathcal{R}}{\mathbf{M}} \frac{T_c}{\gamma} \left(\frac{\gamma+1}{2} \right)^{\frac{\gamma+1}{\gamma-1}}} \tag{26}$$

The system is coherent only if the two expressions give the same result. A system of equations could be created and numerically solved to match both the pressure cascade and c^*.

A reasonable initial guess for chamber pressure $p_c^{(i+1)(1)}$ is taken as the pressure at previous time step $p_c^{(i)}$. The next steps $p_c^{(i+1)(j)}$ will converge progressively towards the real current pressure $p_c^{(i+1)}$ (for increasing j).

From $p_c^{(i+1)(j)}$ the $c^{*(i+1)(j)}$ is computed from the pressure cascade as described in Equation 25:

$$u_{fd,p}^{(i+1)(j)} = \sqrt{\frac{2 \left(p_{pr}^{(i+1)} - p_c^{(i+1)(j)} \right)}{\rho_p K_p}} \tag{27}$$

$$m_p^{(i+1)(j)} = \rho_p A_{fd,p} u_{fd,p}^{(i+1)(j)} \tag{28}$$

$$O/F^{(i+1)(j)} = \frac{m_{ox}^{(i+1)(j)}}{m_{fu}^{(i+1)(j)}} \tag{29}$$

$$c^{*(i+1)(j)} = \frac{A_t p_c^{(i+1)(j)}}{\dot{m}_{fu}^{(i+1)(j)} + \dot{m}_{ox}^{(i+1)(j)}} \tag{30}$$

Equation 26 is solved directly using CEAM software, which takes as input $p_c^{(i+1)(j)}$ and $O/F^{(i+1)(j)}$ to return $c_{cea}^{*(j)}$.

The two computed c^* are then compared: if their difference satisfies a certain tolerance, then the cycle stops and returns the new values for the current time step. Else, the inner cycle continues the refinement by guessing a new $p_c^{(i+1)(j+1)}$ from $p_c^{(i+1)(j)}$.

Finally, a check on the new combustion pressure $p_c^{(i+1)}$ is performed in order to stay above the minimum design pressure $p_{c,min}$, as mentioned in subsection 2.1. Similarly to the previous check, if the pressure drops below the limit the simulation stops and returns the results, else it continues with the next time step.

The same general algorithm is used to refine the initial assumptions of O/F and B, which influence the nominal design of the whole engine (as described in subsection 2.2). In this case, the initial c^* value from design is assumed constant to reduce the computational burden, since the algorithm is applied over a wide range of combinations of O/F and B. This assumption is reasonable because the O/F (and as consequence the thermodynamics of the combustion) hardly varies during the whole burn, as can be noticed in Figure 6.

3 Results analysis

DRY-1 final design, as mentioned in subsection 2.2, maximizes the total specific impulse deliverable while respecting all the constraints and the assumptions of the model discussed in subsection 2.1. It is obtained through the iteration of the code presented in subsection 2.3, varying all the nominal design parameters (geometry included) as function of the selected DOFs: B and O/F. In this part all the losses in the nozzle were neglected. They will be discussed off-design in section 4 to evaluate the behavior of the engine in more realistic conditions. Also the possible non-nominalities in the realization of the injection plate and the possible strategies to cool down the system are separately treated, respectively in section 5 and section 6.

In the present section the obtained design will be presented and analyzed through the most relevant parameters, plotted vs time of burn to see the evolution of the system.

$\overline{O/F}$ [-]	$B_{pr,ox}$ [-]	$B_{pr,fu}$ [-]
2.35	2.78	2.78

Table 11: DRY-1 optimal design values

c^* [m/s]	c_T [-]	T_c [K]	I_{sp} [s]	I_{tot} [Ns]
1856.3	1.932	3692	355.79	$2.173 \cdot 10^6$

Table 12: Performance parameters for DRY-1

$\dot{m}_{fu}$ [kg/s]	$\dot{m}_{ox}$ [kg/s]
$8.322 \cdot 10^{-2}$	$1.956 \cdot 10^{-1}$

Table 13: Mass flow rates for DRY-1

D_t [cm]	D_e [cm]	D_c [cm]	L_c [cm]
1.15	19.88	3.63	11.43

Table 14: Geometry for DRY-1

m_{fu} [kg]	m_{ox} [kg]	$V_{pr,i}^{fu}$ [m³]	$V_{pr,i}^{ox}$ [m³]	$V_{fu,i}$ [m³]	$V_{ox,i}$ [m³]
182.45	428.67	0.2102	0.4441	0.2261	0.3761

Table 15: Tanks sizing for DRY-1
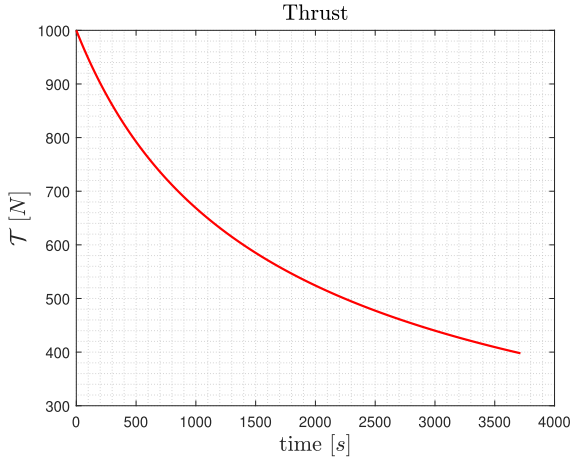
Figure 4: Thrust
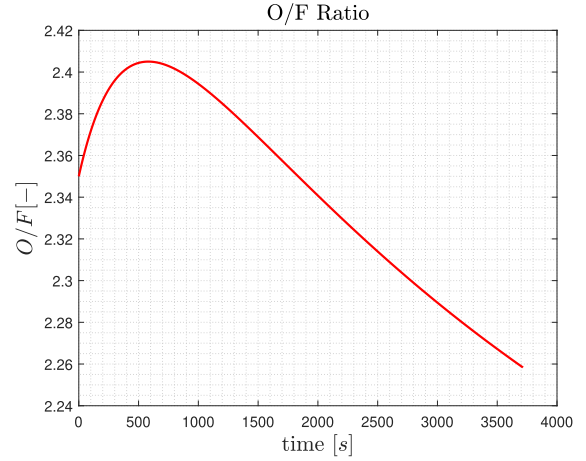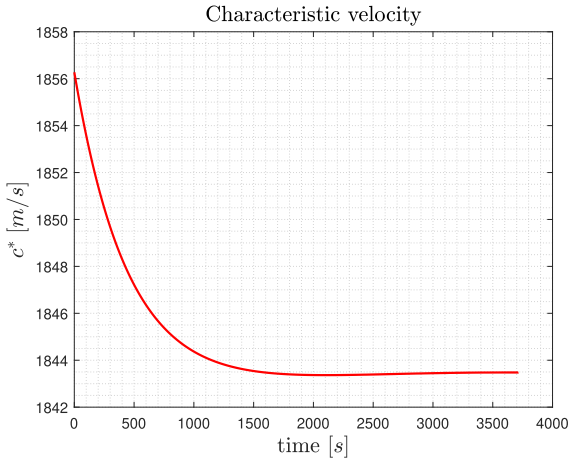

Figure 5: O/F ratio

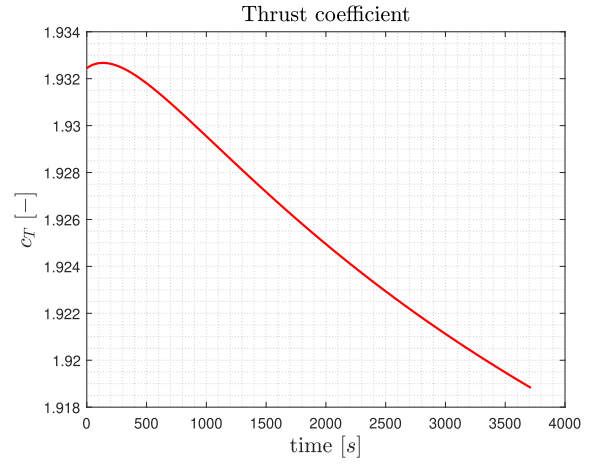Figure 6: Characteristic velocity
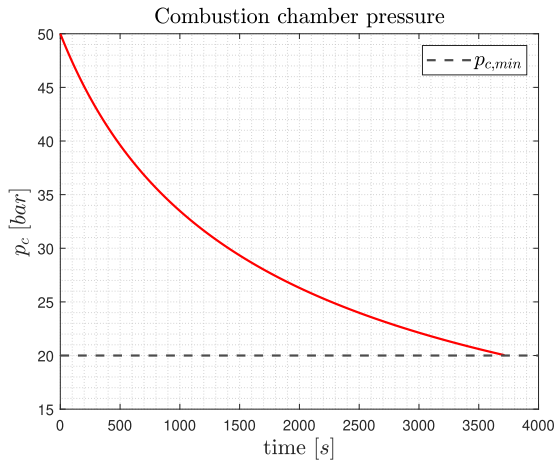

Figure 7: Thrust coefficient
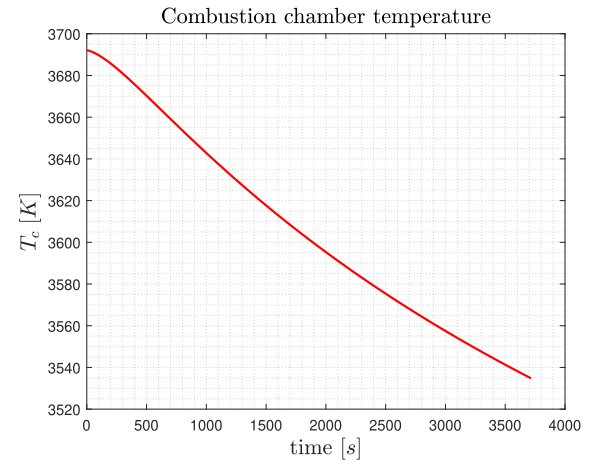

Figure 8: Combustion chamber pressure

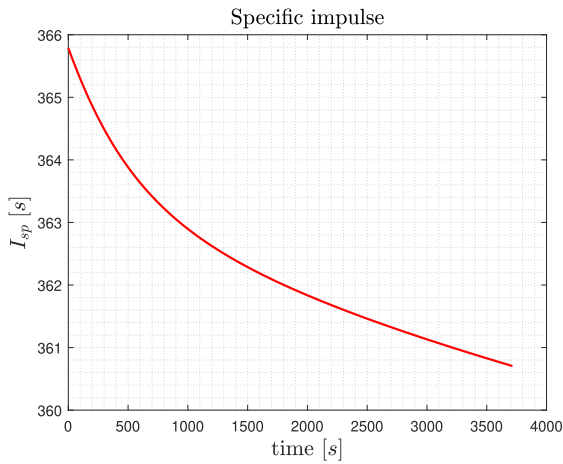Figure 9: Combustion chamber temperature

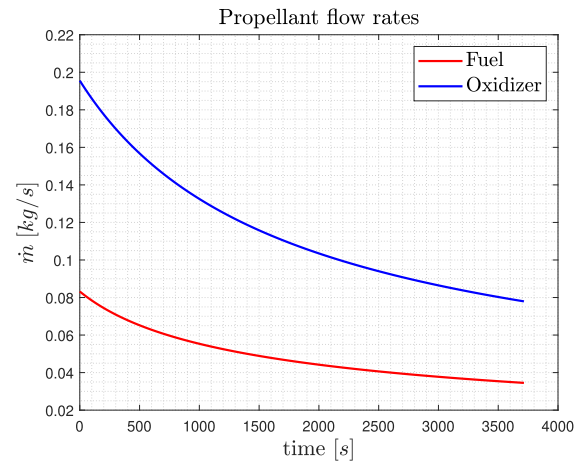Figure 10: Specific impulse

Figure 11: Propellant flow rates

Some general consideration from the graphs can be made.

- The pressure and the temperature in the combustion chamber decreases in time as a consequence of the discharge of the tanks. Thrust and specific impulse diminish as well since they depend on these values.

- Since the combustion is less effective, the characteristic velocity, which depends uniquely on the thermodynamics of the chamber, lower its initial value. Despite this, the global variation is negligible, so it

can be assumed constant to reduce the calculation burden on the dynamics (as already mentioned in subsection 2.3).

- *O/F* ratio barely changes during the time of burn. It has a peculiar evolution with respect to the other monotonic developments: it firstly increases and then decreases. This is mainly imputable to the difference in pressurizers chosen for the two tanks, which have different performances: helium discharges the oxidizer more rapidly with respect to nitrogen, which has a less steep and more constant discharge in time (Figure 11).

- A similar development can be found in the thrust coefficient: this is due to the fact that in vacuum its value depends only by the geometry of the nozzle (which is fixed) and by the specific heat ratio of the exhaust gases. The latter depends on the chemistry of the mixture, but it does not strictly follow the *O/F* ratio.

4 Nozzle losses

In order to calculate and evaluate the nozzle losses, further modifications and calculations were added to the model previously presented in section 2. In particular 2D, throat erosion and boundary layer losses were considered.

4.1 Losses calculations

Each loss term has been calculated as follows:

- **2D losses**: for a parabolic Rao nozzle this loss can be computed in a similar way as a conical nozzle by applying Equation 31

$$\lambda = \frac{1}{2}\left[1 + \cos\left(\frac{\delta + \theta_e}{2}\right)\right] \tag{31}$$

where δ is the cone angle of an fictitious conical nozzle with the same divergent length and area ratio[10].

- **Throat erosion losses:** this effect is due to the increasing throat area over time whose behavior can be obtained by considering a constant erosion rate for simplicity. Since this loss is time dependent it needs to be considered inside the dynamic model of the system (subsection 2.3).

$$D_t^{(i+1)} = D_t^{(i)} + 2E_t\Delta t \tag{32}$$

Usually the erosion rate is calculated through experimental measurements of the propulsion system, in this case a suitable erosion rate has been searched for in literature. Due to the smallness of the system, no acceptable rates were found, therefore an increase of 2% of the initial throat radius over the entire burn was assumed. This gives an erosion rate of about $1.540 \cdot 10^{-2}$ μm/s.[10][16]

- **Boundary layer losses:** to determine this contribution the effect of the boundary layer in the throat of the nozzle must be estimated. To achieve this the thermo-physical properties of the exhaust gasses at the throat must be recovered from the CEAM outputs of the nominal design (subsection 2.2). From them the throat Reynolds number can be obtained.

$$Re_t = \frac{\rho_t D_t u_t}{\mu_t} \tag{33}$$

Introducing the curvature of the throat, recovered from the Rao nozzle geometry, a modified Reynolds number is derived as follows:

$$k_t = 0.382\frac{D_t}{2} \tag{34}$$

$$Re' = \sqrt{\frac{D_t}{2k_t}}Re_t \tag{35}$$

Now it is possible to calculate the throat discharge coefficient from which the real mass flow and effective throat area can be calculated.

$$C_{d,t} = 1 - \left(\frac{\gamma_t + 1}{2}\right)^{\frac{3}{4}} \left[3.266 - \frac{2.128}{\gamma_t + 1}\right] \frac{1}{\sqrt{Re'}} + 0.9428 \frac{(\gamma_t - 1)(\gamma_t + 2)}{Re' \sqrt{\gamma_t + 1}} \tag{36}$$

$$\dot{m}_r = C_{d,t} \, \dot{m}_{id} \tag{37}$$

$$A_{t,eff} = \frac{\dot{m}_r \, c^*}{p_c} \tag{38}$$

4.2 Effects on the nominal design

Including all the losses in the dynamic model reduces the overall performance of the system as expected, however, they only have a minor effect on the evolution of the throat area and its discharge coefficient as can be seen both in Figure 12 and Figure 13. This is mainly due to the fact that the erosion rate was recovered by imposing a rather small variation of the throat area over time.
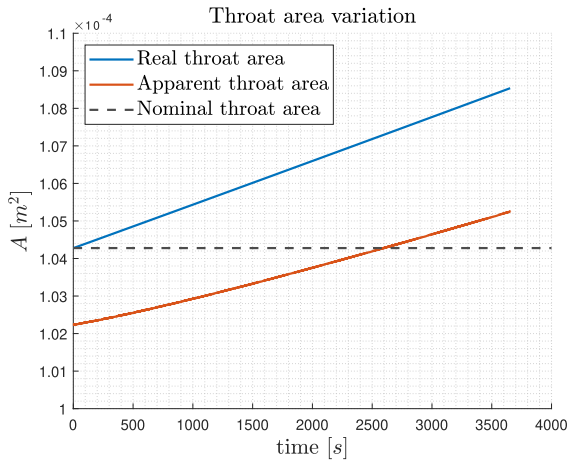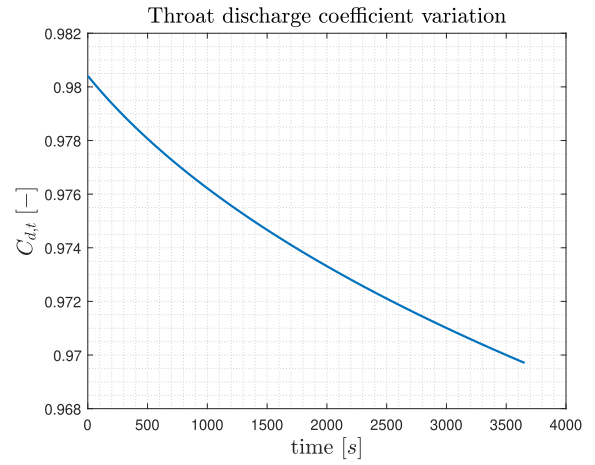

Figure 12: Throat area evolution

Figure 13: Throat discharge coefficient evolution

The real throat area describes its physical evolution due to erosion while the apparent one is the effective area as seen by the gas flow due also to the presence of the boundary layer. The values found for the discharge coefficients, instead, are compatible with values found in literature together with the range of the modified Reynolds number used to compute them.[17] These variations have repercussions over the entire system as the chamber pressure evolution is influenced, so are the pressure cascade, the propellants mass flow rates and all consequent physical quantities as can be seen in the following figures.
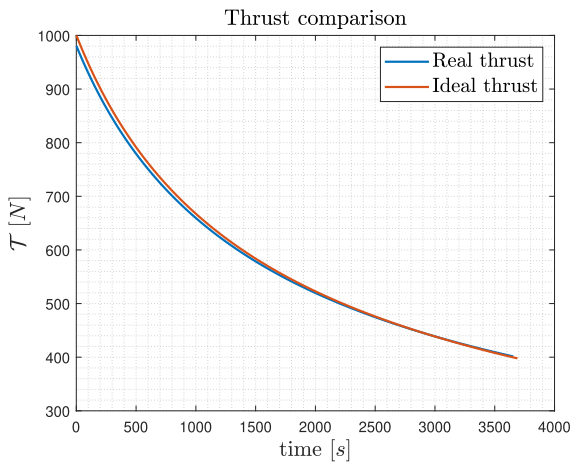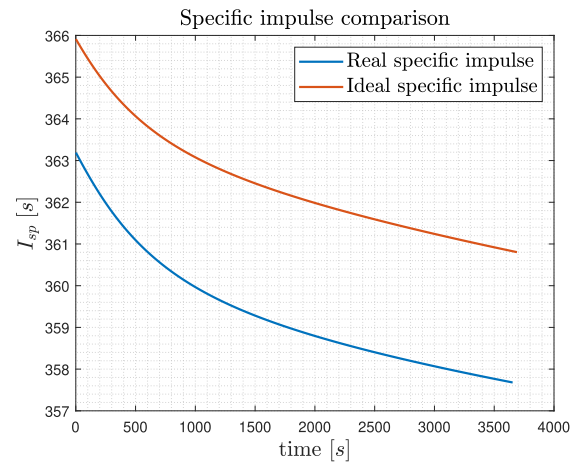

Figure 14: Thrust comparison

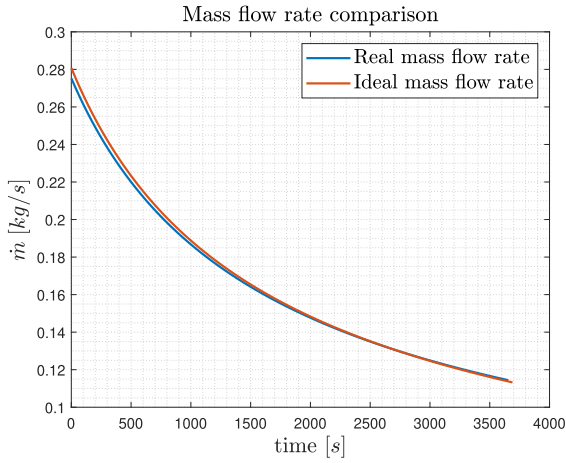Figure 15: Specific impulse comparison

14

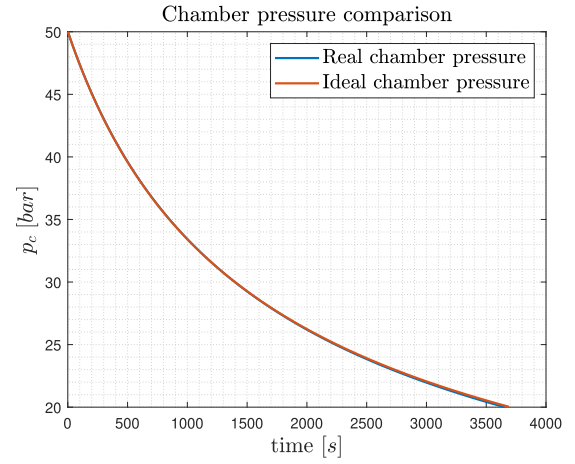Figure 16: Propellants mass flow rate comparison

Figure 17: Combustion chamber pressure comparison

Again it is possible to appreciate the fairly small repercussions of these losses as all quantities exhibit basically the same behavior except the specific impulse, which shows a larger separation from the ideal case. The total impulse and the burn time also decrease slightly as reported in Table 16.

	I_{tot} [N s]	t_b [s]
Ideal	$2.173 \cdot 10^6$	3715
Real	$2.124 \cdot 10^6$	3652

Table 16: Total impulse and burn time comparison

5   Additive manufacturing influences

Additive manufacturing allows to create complex shapes at a lower cost, but it doesn't always allow to obtain low roughness values, causing performance losses in the system. Thus, following the additive manufacturing technology choice explained in subsection 1.2, a value for the discharge coefficient C_d can be estimated from the chart in Figure 18[18], selecting a diameter value of around 1 mm as calculated in section 2 and a short-tube with conical entrance shape.

A further analysis has been developed to take into account possible variations in the injectors' diameters due to imperfections in processing. Inspecting data for laser power bed fusion manufacturing, the standard deviation from a nominal diameter of 1.903 mm is 0.0485 mm[5]. Linearly scaling the value found in literature, it can be adapted for the case analyzed as shown in Table 17.

Figure 18: Discharge coefficients

	Oxidizer injectors	**Fuel injectors**
Nominal diameter [mm]	1.0295	1.0354
Standard deviation [mm]	0.0262	0.0264
Number of injectors [-]	6	3

Table 17: Nominal values and standard deviations for injectors

15

Considering the injectors' diameters as random variables with normal distribution characterized by a mean value and a standard deviation corresponding respectively to the coefficients shown in Table 17, a statistical analysis has been developed to examine the effects of manufacturing imperfections. This random phenomenon causes the variation of multiple propulsion parameters with respect to their nominal value, as will be discussed. Following the diameters' analysis, the total area of both the propellants' injectors has been calculated, to then find the actual mass flow rate entering the combustion chamber and the O/F ratio, all affected by the random variations discussed above.

$$A_{inj,tot,p} = \sum_{n=1}^{N_{inj,p}} \left(\frac{\pi(d_{inj,p,n})^2}{4} \right) \tag{39}$$

$$\dot{m}_{inj,tot,p} = C_d A_{inj,tot,p} \sqrt{2\Delta p_{inj}\rho_p} \tag{40}$$

These modified values then enter the computation explained in section 2, making the uncertainty to propagate and to affect the engine's performance. The whole process is repeated 50 times in order to have a more accurate statistical analysis, allowing to study each simulation and the average of them, as shown in the following graphs.

METTERE I GRAFICI!!!!!!!!
XD LOL XDXDXD
PARLARE PC !!!!!
The mass flow rate, dependent on the injectors' cross sectional area, is slightly affected by the variation of their diameter, very small compared to the nominal one. However, the explained fluctuations can combine generating more observable effects, as seen in ///GRAFICO O/F///, describing the progress of the O/F in time for each simulation. The high deviation from the nominal value is due to its definition as a fraction, greatly affected by the combined variations of its terms. O/F is a crucial parameter in the design of a propulsion system, from which many other variables depend. T_c is one of them, being obtained from the NASA-CEAM software, which, among others, takes as input the O/F ratio and the combustion chamber pressure, P_c, that is related to the tank pressure through the injectors' areas and hence varying due to the analyzed imperfections. Thrust and specific impulse are also strictly related to the variation of mass flow rate and, as a consequence, the oxidizer to fuel ratio.

Another characteristic worth to mention is the convergence of all parameters to their mean value during each simulation. In fact, as shown in Equation 19 the difference in pressure depends quadratically on the varying flow velocity, which is the highest in the first instants of simulation. For this reason, the effect of imperfections is clearly distinguishable from (grafico salti di pressione), where, as u_{fd} and thus the mass flow rate diminish, the difference between the Δp_{fd} of each simulation and their average lowers, as the effect of the imprecision in diameter due to the manufacturing process gets less relevant. The shown graph is derived from oxidizer feed lines values as no conceptual difference was found from the fuel's one.

Given the hypothesis made in subsection 1.1, the whole system is regulated by the the choice of pressurizer, the blow-down and the $\overline{O/F}$ ratios: the natural evolution of the dynamics leads to a common and defined state among all simulations.

The analyzed parameters' trend is dictated by chemistry and by the blow-down ratio, as they regulate the discharge process of the propellants, while their boundaries are only determined by the $\overline{O/F}$ value. All the simulations behave coherently with these assumptions.

6   Cooling analysis

In this section a preliminary feasibility analysis for cooling of the DRY-1 engine with RP-1 is discussed. High temperatures reached in the combustion chamber and nozzle have to deeply discussed at this first stage of the design since it could have deep consequences on the architecture, materials choice and performances of the

engine. The following analysis is necessary to evaluate the researched feasibility of RP-1 as a coolant. In this context, it is possible to make reference to past successful engine design since kerosene cooling has been of fundamental importance for vast applications.

Two kinds of techniques could be considered with this propellant, regenerative cooling and film cooling. The last one is used along the lateral surface of the combustion chamber to create a fuel layer that protects the chamber, with a slight decrease on the performance. This strategy has demonstrated great effectiveness for in-space and low pressure engines[19], an example of this is given by the previously cited 400-N Liquid Rocket engine for in-space applications[11]. DRY-1 could exploit film cooling as a viable option thats is also enhanced by previous successful design for this small-thrust kind of motor. Clearly, the feasibility shall be quantitatively assessed.

On the other way, regenerative cooling techniques are not frequently seen on small thrust or low pressure chamber pressure applications since the critical point of the process relies on having sufficient pressure for the fuel line that is affected by losses along the cooling jacket. Considering the DRY-1 blow-down architecture, the critical points would be:

- **Fuel feeding line pressure losses**: the pressure in the lines of feeding is varying along the operation, in particular at the end of the mission low fuel pressure could not match the requirement of pressure at the combustion chamber.

- **Variation of boiling temperature**: due to variation of fuel feeding pressure, also the vaporization temperature varies. In general temperature shall be assessed through the pipes to evaluate if decomposition or vaporization of RP-1 is happening.

6.1   Mathematical model for the gas heat transfer

The workflow of this section is to evaluate whether the total heat flux generated by the gas flow (as convective heat) can be absorbed by the coolant without exceeding temperature constraint of the RP-1. Different approaches and assumptions can be made to breakdown the problem. In this case it is assumed to have a one-dimensional flow (perpendicular to the expanded gas flow), the heat is exchanged only by forced convective processes (disregarding the radiation coming from the flow), steady state assumption is made. Some other assumptions will be presented during the following development. Regarding the model of convective heat transfer from the hot gases to the wall, it can be mathematically described as:

$$\dot{q} = h_g(T_{aw} - T_{wg}) \tag{41}$$

The temperature considered for the gas flow T_{aw} is referred as the total adiabatic wall temperature and is calculated as:

$$T_{aw} = T_c \left[\frac{1 + r\left(\frac{\gamma-1}{2}\right)M^2}{1 + \left(\frac{\gamma-1}{2}\right)M^2} \right] \qquad r = Pr^{0.33} \tag{42}$$

Where Mach number is the one relative to the axial distance, in which T_{wg} has to be calculated, the recovery factor r depends on the local Prandtl number. Also γ is assessed at axial coordinate of interest. T_{wg} is the static temperature of the wall on the internal side. T_{aw} is the temperature driving the heat transfer and it is slightly less then stagnation temperature of the gas due to the back heat effect generated by the compressible and viscous boundary layer near the chamber wall. The difficulty relies on establishing the value of the convective heat transfer h_g, different empirical models are present in the literature. One of the most used and commonly applied is the Bartz relation given as:

$$h_g = \left(\frac{0.026}{D_t^2} \right) \left(\frac{\mu^{0.2} c_P}{Pr^{0.6}} \right)_c \left(\frac{p_c}{c^*} \right)^{0.8} \left(\frac{D_t}{k_t} \right)^{0.1} \left(\frac{A_t}{A} \right)^{0.9} \sigma \tag{43}$$

$$\sigma = \frac{1}{\left[\frac{1}{2} \frac{T_{wg}}{T_c} \left(1 + \frac{\gamma+1}{2} M^2 + \frac{1}{2} \right) \right]^{0.68} \left[1 + \frac{\gamma-1}{2} M^2 \right]^{0.12}} \tag{44}$$

Regarding Equation 43, it depends on the geometry of the nozzle and chamber conditions. The area ratio of the same formula gives the dependence on the axial distance. The factor σ in Equation 44 is also dependent on the axial distance of the nozzle since it contains the Mach number and the temperature of the wall on the gas side at that location. In the same equation, γ is also referred to the local value at that position. It can be noticed that the unknown temperature T_{wg} is present also in the h_g coefficient: an assumption on the wall temperature must be taken. In particular, when the material of the nozzle wall is defined, also a maximum allowed temperature is provided. A reasonable assumption for the adiabatic temperature distribution T_{wg} can be done assuming that the ratio $T_{wg}(x)/T_{aw}(x)$ is constant and equal at the same ratio evaluated at the nozzle inlet, imposing $T_{wg} = T_{max}$ at the nozzle entrance. In Figure 19 it is represented the distribution of the assumed T_{wg} along the nozzle.
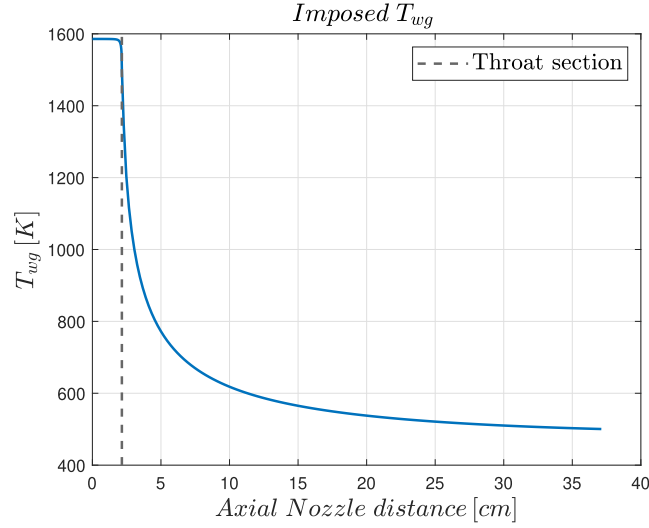

Figure 19: Assume distribution for the wall temperature at the gas side

The maximum allowed temperature for the wall side is at the inlet of the nozzle. The material selected is Nimonic Alloy 75, a nichel-chromium alloy with maximum allowed temperature of 1600K[20]. Hence, this value was set as the T_{wg} at the nozzle inlet. A more conservative approach should consider also lower values of the maximum reachable wall temperature to account for the decrease of material mechanical properties,
In this way, from the calculation of h_g also the heat flux along the nozzle can be evaluated, from the convergent to the exit section. The total heat rate can be estimated by integrating the heat flux over the internal area of the nozzle. This value can be found by numerical integration and the use of the Rao nozzle geometry introduced in subsection 2.2. Finally, the increase of temperature of the fuel can be found by assuming the specific heat of the liquid.

$$\dot{Q} = \int_0^{L_{tot}} \dot{q}\,dx \tag{45}$$

$$\Delta T_{fu} = \frac{\dot{Q}}{c_{fu}\dot{m}_{fu}} \tag{46}$$

At this point, another consideration has to be pointed out: the condition that was set up by imposing the gas side wall temperature at its maximum (depending on the material choice) is a conservative choice since at the steady state it is related to the minimum flow that will be absorbed by the coolant (assuming fixed stationary gas flow conditions). If the coolant would not withstand this condition, the regenerative cooling could be excluded or eventually some other material or coating shall be used for the nozzle. Moreover, the blow-down architecture of the DRY-1 engine implies the reduction of the chamber pressure. This has major consequences on the heat transfer coefficient for the gas side. As a rule of thumb the h_g depends linearly on thrust chamber pressure, when this last value decrease the heat flux will also decrease (considering the same maximum wall temperature).
The heat transfer evaluation has also been combined with the system discharge dynamics (considering c^* as constant) in order to evaluate the heat flux rate, the heat rate and the increase of temperature for the fuel at every instant.

$\Delta T_{co,1}$ [K]	$\Delta T_{co,2}$ [K]	$\Delta T_{co,3}$ [K]
804.13	987.61	990.53

Table 18: Coolant increase of temperature considering three time instants
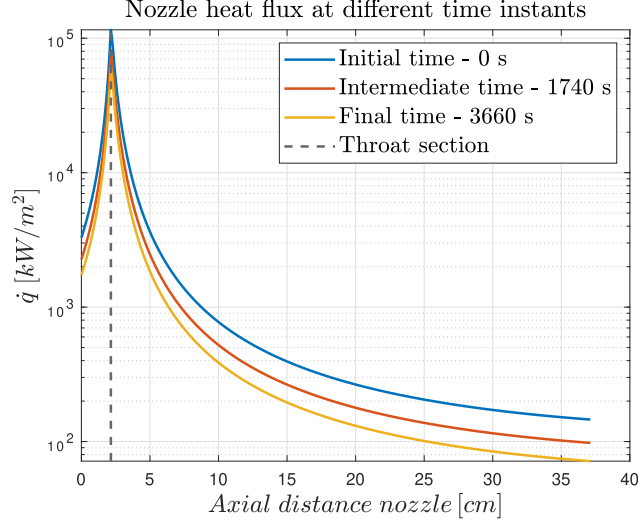

Figure 20: Heat flux along the nozzle at different time instants

From Table 18 it can be understood that the propellant mass flow rate of the fuel is not enough to absorb the heat without having several effects. Two opposite effect happens during the discharge of the blow-down: the decrease of the convective heat transfer coefficient related to the chamber pressure, but also the decrease of the propellant mass flow rate. The latter effect is prevailing since the increase of ΔT_{co} is larger at later time instants. Such high values of ΔT_{co} would bring to vaporize the fuel considering that the storing temperature of the RP-1 is 300 K (boiling temperature for RP-1 happens in the range 623K - 798K[21]). At high temperature decomposition process for the RP-1 can take place. Regarding the nozzle cooling, the radiative capability of the external wall shall be computed, also some other kinds of material or TBC for the internal wall such as ZrO_2 should be investigated. Summing up the result of the present investigation, it can be stated that regenerative cooling for such a small-sized engine as it is the DRY-1 could be excluded due to three critical aspects:

- High heat fluxes due to the miniaturization $h_g \propto D$. Considering motor with the same combustion initial conditions (same couple, P_c and O/F), smaller engines will have to face more critical heating conditions;
- reduced mass flow rate of the fuel induces high ΔT_{co} to ensure power conservation;
- blow-down dynamics creates different conditions throughout the burn.

Concerning the cooling of the thrust chamber, a viable option could be the introduction of a film cooling layer across the internal wall of the combustion chamber. The usage of hydrocarbon-based coolant with this technique revealed effective results. Under pressure of 130 bar, the hydrocarbons deposit acts as a thermal insulator hence protecting the walls of the chamber[12]. In addition, the design of the film cooling should consider the re-design of the injector plate and should be evaluated in parallel with the material choice for the combustion chamber.

19

Bibliography

[1] Robert-Jan Koopmans et Al. "Propellant Tank Pressurisation with Helium Filled Hollow Glass Microspheres". In: (2015).

[2] H. C. Hearn. "Design and Development of a Large Bipropellant Slowdown Propulsion System". In: (1995).

[3] Filippo Berto et al. "Metal additive manufacturing in aerospace: a review". In: (2021).

[4] *Inconel vs Stainless Steel*. Site: `https://markforged.com/resources/blog/inconel-vs-stainless-steel`.

[5] Dalia Mahmoud et al. "Applications of Machine Learning in Process Monitoring and Controls of L-PBF Additive Manufacturing: A Review". In: (2021).

[6] M. A. Balbaa et al. "Role of powder particle size on laser powder bed fusion processability of AlSi10mg alloy". In: (2021).

[7] Thomas Dahmen. "Additive Manufacturing For Fuel Injectors: Design, Processes and Materials". MA thesis. DTU, May 2021.

[8] Amir Mostafaei et al. "Binder jet 3D printing—Process parameters, materials, properties, modeling, and challenges". In: (2021).

[9] *What it binder jetting?* Site: `https://markforged.com/resources/blog/inconel-vs-stainless-steel`. 2024.

[10] G. P. Sutton. "Rocket Propulsion Elements". In: (2017).

[11] Ariane Group. *Chemical bipropellant thruster family*. Site: `https://www.space-propulsion.com/`. 2021.

[12] Huzel and Huang. "Modern Engineering for design of Liquid-Propellant Rocket Engines". In: (1992).

[13] G. V. Rao. "Exhaust Nozzle Contour for Optimum Thrust". In: (1958).

[14] *NIST Chemistry WebBook*. URL: `https://webbook.nist.gov/cgi/fluid.cgi?T=85&PLow=4&PHigh=5.5&PInc=0.1&Digits=5&ID=C7727379&Action=Load&Type=IsoTherm&TUnit=K&PUnit=bar&DUnit=mol%2Fl&HUnit=kJ%2Fkg&WUnit=m%2Fs&VisUnit=Pa*s&STUnit=N%2Fm&RefState=DEF`. (accessed: 14.04.2024).

[15] Ajinkya A. More. "Analytical solutions for the Colebrook and White equation and for pressure drop in ideal gas flow in pipes". In: (2005).

[16] Mohd Aizat Iz'aan Mohd Ali et al. "Investigation on Nozzle Throat Erosion in Hybrid Rocket Motor due to Nozzle Expansion Ratio". In: (2023).

[17] Filippo Maggi. "Space Propulsion course slides". In: (2024).

[18] Michael C. Waters. "Analysis of Additively Manufactured Injectors for Rotating Detonation Engines". In: (2018).

[19] Stephen D. Heister. "Rocket Propulsion". In: (2019).

[20] Special Metals. *Nimonic Alloy 75*. Site: `https://shorturl.at/ctzV7`. 2004.

[21] Tim Edwards. "Liquid Fuels and Propellants for Aerospace Propulsion". In: (2003).